Katharine K. Ferster[1]
Mem. ASME
Department of Mechanical and
Nuclear Engineering,
The Pennsylvania State University,
3127 Research Drive,
State College, PA 16801
e-mail: kkf5066@psu.edu

Kathryn L. Kirsch
Mem. ASME
Department of Mechanical and
Nuclear Engineering,
The Pennsylvania State University,
3127 Research Drive,
State College, PA 16801
e-mail: kathryn.kirsch@psu.edu

Karen A. Thole
Mem. ASME
Department of Mechanical and
Nuclear Engineering,
The Pennsylvania State University,
136 Reber Building,
University Park, PA 16802
e-mail: kthole@psu.edu

Effects of Geometry, Spacing, and Number of Pin Fins in Additively Manufactured Microchannel Pin Fin Arrays

The demand for higher efficiency is ever present in the gas turbine field and can be achieved through many different approaches. While additively manufactured parts have only recently been introduced into the hot section of a gas turbine engine, the manufacturing technology shows promise for more widespread implementation since the process allows a designer to push the limits on capabilities of traditional machining and potentially impact turbine efficiencies. Pin fins are conventionally used in turbine airfoils to remove heat from locations in which high thermal and mechanical stresses are present. This study employs the benefits of additive manufacturing to make uniquely shaped pin fins, with the goal of increased performance over conventional cylindrical pin fin arrays. Triangular, star, and spherical shaped pin fins placed in microchannel test coupons were manufactured using direct metal laser sintering (DMLS). These coupons were experimentally investigated for pressure loss and heat transfer at a range of Reynolds numbers. Spacing, number of pin fins in the array, and pin fin geometry were variables that changed pressure loss and heat transfer in this study. Results indicate that the additively manufactured triangles and cylinders outperform conventional pin fin arrays, while stars and dimpled spheres did not. [DOI: 10.1115/1.4038179]

Introduction

The design opportunity offered through direct metal laser sintering (DMLS) is an attractive feature of the manufacturing method. In addition to being able to use materials that can withstand harsh environments, such as the hot section of gas turbine engines, the DMLS method allows the production of complex shapes on a micro-scale. One application of these micro features comes in skin cooling of gas turbine components.

Despite the wide range of design possibilities available within DMLS, a new cooling technology should perform as well or better than its conventionally manufactured counterpart. In situations where large mechanical stresses and high heat loads affect a part, the cooling scheme must provide mechanical strength while maintaining acceptable part temperatures. Generally, pin fin heat exchangers perform well in such roles. Traditionally, these pin fins have been round pins but with the advent of DMLS, more complex shapes are made possible: a DMLS pin fin array no longer needs to take the form of a cylindrical pin fin array.

Three different shapes of pin fins were studied for this paper: triangular, star, and dimpled spherical pins. Pin fins work to disrupt the boundary layer on the endwall surfaces as well as increase the surface area over which heat transfer can take place. The chosen geometries were hypothesized to strongly affect the wake patterns in the arrays and, in the case of the stars and the dimpled spheres, greatly increase the convective surface area. Array configurations were such that three test campaigns could be completed: (1) matched spanwise and streamwise spacing among the three pin fin shapes, (2) matched convective surface area in each of the pin fin arrays, and (3) varied spanwise and streamwise spacing for the triangular and star shaped pin fins.

The goals of the current study are to assess the capabilities of the DMLS process to produce a microarray of discrete, complex shapes and to understand how the process affects the friction factor and heat transfer performance. Additionally, the shape and performance of the current arrays will be compared to DMLS cylindrical pin fin arrays from Kirsch and Thole [1].

Literature Review

The study of pin fin heat exchangers has generated much interest across multiple research groups over many years. Common parameters to vary in a pin fin array are pin height-to-diameter (H/D) ratios [2], spanwise spacing (S) and streamwise spacing (X) [3–5], array orientation [6], and the number of pin fin rows [7,8]. Spanwise spacing, conventionally normalized by pin diameter, strongly affects the pressure drop across an array because it dictates the number of pins that serve as blockages to the flow [4,7]; tighter spanwise spacing leads to higher friction factors. Streamwise spacing, on the other hand, more strongly affects the heat transfer in the array because it influences the wake interactions in the channel [8,9]. Ostanek and Thole [10] performed flowfield studies in pin fin arrays and found that when $X/D \leq 2.6$, typical vortex shedding behavior was suppressed.

Cylindrical pin fins are the most common pin fin shape and are the most practical to implement in gas turbine applications [11]. However, some studies have looked at the effect of changing the pin shape on the array performance. Uzol and Camci [12] found that elliptical pins yielded lower friction factor and heat transfer when their long axes aligned with the flow direction, in comparison to pin fin arrays. However, the thermal performance of the elliptical pins, measured as $(\mathrm{Nu}/\mathrm{Nu}_0)/(f/f_0)^{1/3}$, was equaled to that of the cylindrical pins. Chyu et al. [13] studied cubic and diamond shaped pin fins; the sharp corners on the pins generated higher turbulence in the channel, which was beneficial to the heat transfer. Kirsch et al. [14] looked at one row of oblong pins in a multirow array of cylindrical pins. The flow around the oblong pins positively affected the heat transfer from cylindrical pin rows

[1]Corresponding author.

Contributed by the International Gas Turbine Institute (IGTI) of ASME for publication in the JOURNAL OF TURBOMACHINERY. Manuscript received August 27, 2017; final manuscript received September 10, 2017; published online October 31, 2017. Editor: Kenneth Hall.

downstream. İzci et al. [15] numerically investigated microarrays of triangular, diamond, square, rectangular, and conical shaped pins with Reynolds numbers ranging between 20 and 120; the rectangular pin shape provided the highest fin efficiency. Siw et al. [16] studied triangular and semicircular shaped pin-fin arrays and compared the results to cylindrical pin fins. The triangular pins were oriented with their point facing the flow direction. The authors found that triangles generated the highest heat transfer augmentation while the semicircular pins showed low heat transfer performance. However, the triangles also induced the largest pressure loss.

Other studies have sought to capture the effects of microchannel pin fin arrays as they compare to their scaled-up counterparts. Marques and Kelly [17], for example, manufactured micro pin fin arrays using the LIGA (lithography, electroplating, and molding) micromachining process and found that the performance of the microarrays matched that of scaled-up arrays with the same normalized spacings. Heo et al. [18] used deep reactive ion etching to roughen micro pin fin arrays ($\epsilon/D_h = 0.035$) and compared the heat transfer and pressure loss from the roughened array to smooth ones in the laminar regime ($70 < \mathrm{Re} < 250$); the roughness increased the heat transfer over a smooth array only at tight spanwise and streamwise spacings ($S/D = X/D < 1.3$).

Jodoin and associates [19–21] used cold spray additive manufacturing to build pin fin arrays containing pyramidal pin fins. μ-particle image velocimetry measurements showed that the high surface roughness, a consequence of the manufacturing process, caused an early transition to turbulence; turbulence intensities were quoted up to 25% for a Reynolds number of 500 [20]. Dede et al. [22] applied the selective laser melting technique to build a finned external flow heat exchanger and found the roughness to be beneficial to the heat transfer. Kirsch and Thole [1] used DMLS to build pin fin arrays containing cylindrical pin fins and found that the channel roughness was a function of the number of pins in the channel. More pins in the channel promoted higher heat accumulation during the build, which attracted more loose powder particles to adhere to the endwall and pin surfaces. Jamshidinia and Kovacevic [23] reported similar findings from a DMLS build: parts in close proximity to one another during a build showed higher roughness than isolated parts.

Surface roughness in the DMLS process is a strong function of machine parameters such as laser power [24], laser energy density [25], and layer thickness [26], as well as laser scan speed, hatch spacing, and laser path [27–29]. Snyder et al. [30] cited build direction as having a significant influence on both surface roughness and the ability of the DMLS process to reproduce a given computer-aided design (CAD) model; these findings were corroborated in separate studies by Delgado et al. [28], Pakkanen et al. [31], and Bacchewar et al. [24].

Especially at the micro scale, evaluation of the as-built internal features of a part is critical to data reduction because the final part may differ by up to 10% from the CAD model [32]. A common method for nondestructive evaluation of parts is to use a computed X-ray tomography (CT) scan [30,33,34]. For characterization at higher resolution, a scanning electron microscope [35–37] or optical profilometer [35,37] can be used, but requires line of sight and is therefore ill suited for investigating internal channels.

Previous studies have shown a widespread interest in advanced manufacturing technologies, such as DMLS. Of particular interest is the application of DMLS in gas turbine engines. More stringent efficiency requirements resulting from harsher working environment conditions continue to drive the need for finned heat exchangers. This study is unique in that it exploits the manufacturing capabilities of DMLS to enhance and improve a common, yet effective means of maintaining component durability.

Descriptions of Test Coupons

Test coupons of uniquely shaped pin fin geometries and various spacings were additively manufactured using DMLS from stock Inconel 718 powder; the pin shapes are shown in Table 1. The machine parameters were set to the default parameters for Inconel 718 [38]. For ease of comparison, the coupons were made with the same parameters as a previous study done on cylindrical pin fins [1]. The height and length of each coupon were 1.5 mm and 25.4 mm, respectively, with the height of the microchannel containing the pins at 1.0 mm. Additionally, flanges were manufactured at the inlet and exit of the microchannels to act as the point of contact between the test coupon and testing facility.

Table 1 Partial view of matched surface area coupons

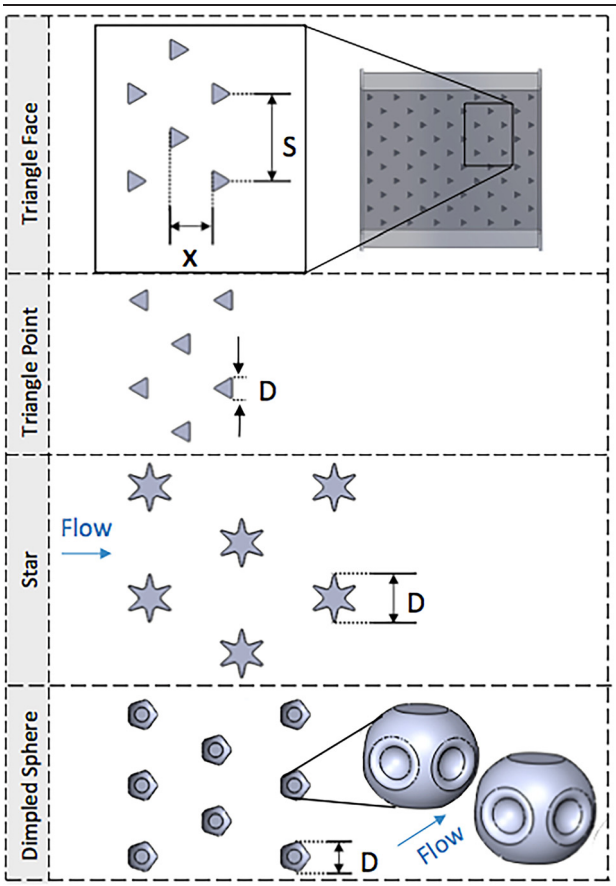

During the manufacturing process, the coupons were built at 45 deg to the horizontal. For Inconel 718, the minimum required angle for sufficient layer support was 40 deg; building the test coupons at 45 deg ensured that all downward facing pin surfaces would build appropriately. Before testing, the coupons were first stress relieved, then removed from the build plate using wire electro discharge machining. To ensure proper fit in the testing facility, the exterior of each coupon was sized and smoothed.

In total, eleven pin fin arrays were printed: five triangular, four star, and two dimpled spherical arrays, which were chosen for their aerodynamic properties and/or surface area addition. Three different studies were performed to see how matched spacing, matched surface area, and varied spacing affected the pressure loss and the heat transfer. Spacing of the pins was denoted by X and S, which stand for streamwise and spanwise, respectively.

Table 1 labels the spacing and diameter, chosen as the maximum dimension obstructing flow, of each coupon with matched surface area. A comparison between the geometries and size can be made since the figures are oriented from a datum and are drawn to scale. Only three rows of each shape are shown, but the coupons all contained multiple rows; Table 2 quantifies the number of rows in each test coupon. The triangle face features the full array on the right to show that the table is only a partial view. The observation of note is that each geometric shape obstructs various

Table 2 Dimensions, spacings, and rows of coupons printed

Geometry	Triangle		Star		Dimpled sphere		Cylinder [1]	
Diameter (mm)	0.93		2.2		1.44		1.0	
Spacing	Number of pins in:		Number of pins in:		Number of pins in:		Number of pins in:	
	X	***S***	***X***	***S***	***X***	***S***	***X***	***S***
$S/D = 1.5, X/D = 1.3$	21	14	9	7			19	13
$S/D = 1.5, X/D = 2.6$	11	14	5	7			9	13
$S/D = 2.0, X/D = 2.6$	11	11	5	5	7	7	9	9
$S/D = 4.0, X/D = 2.6$	11	6					9	5
Matched Surface Area Spacing	11	5	6	4	7	6	9	9
	$S/D = 4.4, X/D = 2.1$		$S/D = 2.3, X/D = 2.1$		$S/D = 2.4, X/D = 2.1$		$S/D = 2.0, X/D = 2.6$	

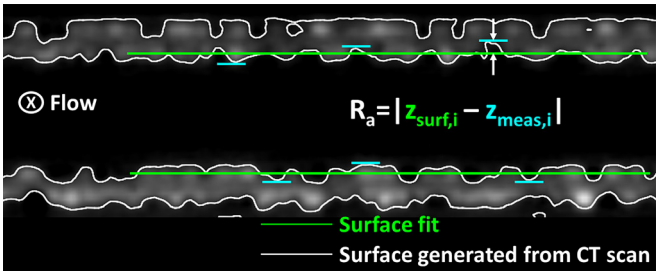

Fig. 1 Depiction of surface roughness calculations with two-dimensional (2D) slice

amounts of flow with the triangular pin being the smallest and star the largest. Table 1 also contains an isometric view of the dimpled sphere; the sphere radius was chosen such that the pin footprint area would be equaled to that of the cylindrical pin from Ref. [1]. Five dimples (represented by concentric circles) were imprinted evenly around the circumference. The maximum imprint depth of the dimples was 0.25 mm.

Table 2 lists the diameter, spacings, and number of pins in spanwise and streamwise direction printed for the geometries. The spacings are listed as X/D and S/D, or the streamwise and spacing dimensions normalized by the pin diameters. Coupons of the same spacing, of the same geometry, and of the same surface area will be compared. To note, the widest spacing of the star pin fins was manufactured, but will not be included in the results. The wide spacing resulted in too few pins in the channel to support the top endwall fully, which resulted in portions of the endwall caving into the channel slightly. Therefore, the results from that coupon would not be comparable to the other test coupons, whose endwalls were flat.

Fin efficiency was calculated for each shaped pin, as was an overall surface efficiency for each array of pins by using the methods prescribed in Ref. [39]. Each pin exhibited a fin efficiency of over 91%, though each pin array exhibited an overall surface efficiency greater than 99%.

Geometric Characterization

Previous studies showed that the DMLS process produces rough surfaces and the final product can deviate from CAD models within tolerances governed by machine parameters [30]. To complete an accurate analysis, it is important to expose the internal surface roughness, area, and build accuracy of the DMLS process. Three coupons from the current test matrix were analyzed in detail to understand how well the different shapes could be reproduced. While different pin spacings have been shown to affect the levels surface roughness in the channels [1], the discussion in the experimental results section will be motivated more by the difference in pin shapes than the differences in relative roughness of the channels. The three coupons that were chosen contained the same normalized spanwise and streamwise spacing.

Images of the interior of the three coupon geometries were taken using a CT scanner and are displayed in Fig. 1, as a 2D slice, and Fig. 2, as a three-dimensional (3D) rendering coupled with a 2D slice. A study previously done on cylindrical pin fins characterized the coupons that same way and will be included here for comparison [1]. To quantify surface roughness, a polynomial surface was fit to both top and bottom endwalls, the complex shapes of which were described using a dense point cloud that captured all peaks and valleys resulting from the roughness features. Through an in-house code, the difference between the surface point cloud and the surface fit was calculated to determine an arithmetic mean roughness value, R_a, used in the analysis of the CT scan data was capable of resolving surface boundaries within 3.5 μm, which was 1/10th the resolution of the CT scan itself. The surfaces of all coupons were determined using the algorithms within the analysis software; the white outline shows an example

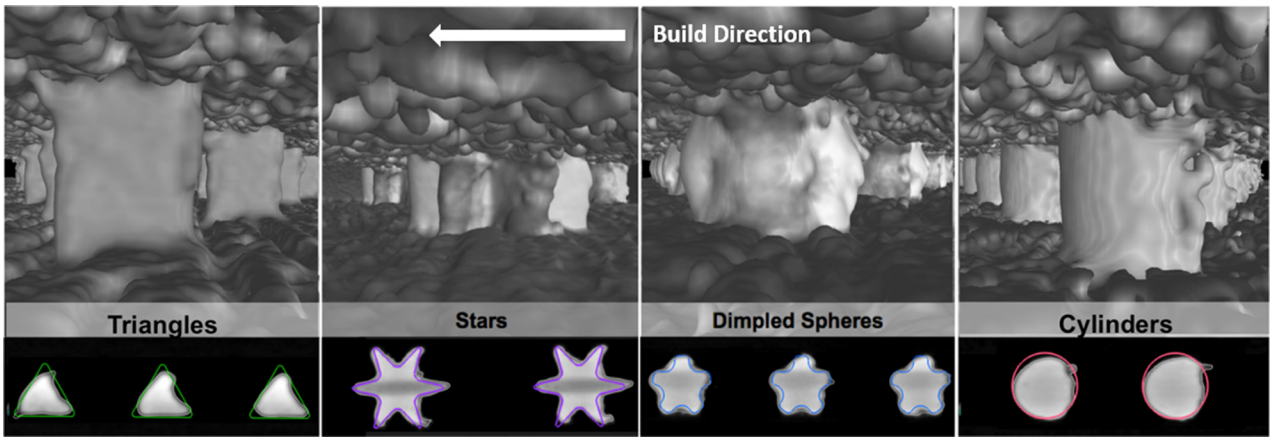

Fig. 2 Three-dimensional images of the internal channel for each pin shape, along with a 2D slice of the coupons with the corresponding CAD models

of the surface determination and the green line shows an example of the mean surface, z_{surf}. The arithmetic mean roughness, therefore, was calculated as the measured surface, as determined using the CT scan software, and the mean surface. The gray region represents the solid area and the black region represents the area open to flow. No pins are pictured in Fig. 1.

A significant difference between DMLS microchannels filled with pin fin arrays and DMLS microchannels without pin fin arrays comes in the amount of material that makes up the heat exchanger, where microchannel walls run the length of a test piece, pin fin arrays contain multiple open, unsupported sections between pin fin rows and columns, depending on the pin spacing. This characteristic of pin fin arrays has implications for the roughness features that form during the build process: where the endwalls are unsupported by pin fins, heat pickup in the area leads to higher roughness. In Fig. 2, visual inspection of the roughness on both top and bottom endwalls shows similarities in the roughness levels, which indicates that the pin wake interaction with the endwalls would be equally affected by the roughness features.

Each of the pin diameters were calculated along with the roughness levels in each channel from the CT scan data and are shown in Table 3. The size of the roughness features in each of the coupons was about 5% of the channel hydraulic diameter. In general, the pin diameters were slightly smaller than their intended design, with the exception of the star pin. Due to the chosen build direction, one point of the star was unsupported during the build and consequently, built longer than intended, creating a slightly wider blockage in the channel. Figure 2 exemplifies the ability of the DMLS process to replicate the different pin geometries. Each of the 2D slice images was taken at 50% the channel height. The 3D images were taken from inside the 3D rendering of the CT scan 2D slices; the top wall in each of the images was the top endwall during the build. The large roughness features on both the endwalls and the pins themselves in each of the four images are evident, as is the unique shaped pins for each of the cases. As expected, the points on the triangular and star pins are not as sharp as their CAD models', but their general shapes held true. The imprint of the dimples on the spherical pin was a mere 0.25 mm, but built reasonably well on both upward and downward facing surfaces.

Experimental Setup

The test facility, shown in Fig. 3, was used to conduct both flow and heat transfer tests for these experiments. Previous studies from our laboratory have also used this facility [30,33,34,40]. The facility depended on air flow that originated from a constant pressure inlet and the flow rate was set to achieve the target Reynolds number. Various sized pressure transducers were used so that a range of Reynolds numbers between 300 and 30,000 could be reached to measure the pressure drop through the test coupon. The Reynolds number definition used for these tests is shown in Eq. (1) and uses the maximum velocity in the channel as the scaling velocity and the pin diameter, chosen as maximum blockage of the channel, as the characteristic length scale. The maximum velocity in the channel was calculated as a function of the mean channel velocity using Eq. (2), where W represents the channel width and N_{span} is the number of pins in the spanwise dimension.

Table 3 Pin diameters and roughness values measured from CT scan

	$S/D = 2.0, X/D = 2.6$			
	Triangular	Star	Dimpled sphere	Cylindrical [1]
D (mm)	0.8	2.3	1.2	0.9
R_a/D	0.11	0.04	0.07	0.08
R_a/D_h	0.05	0.05	0.04	0.05

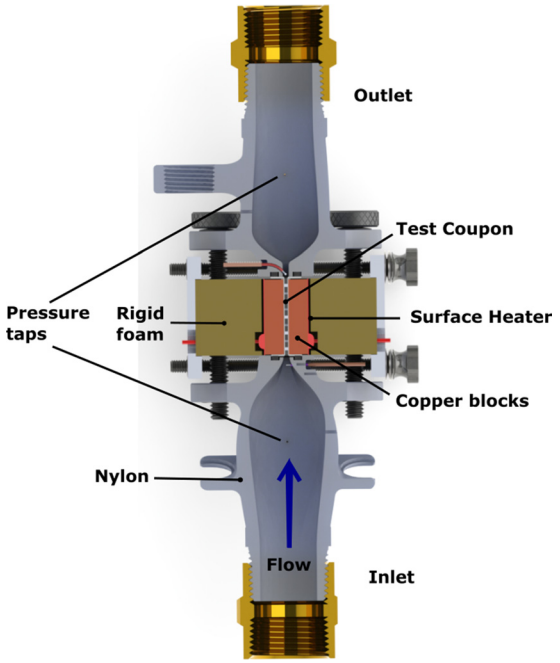

Fig. 3 Test facility used for flow and heat transfer tests

The mean velocity was calculated from the known mass flow rate into the system, governed by a commercial gas flow controller [41]

$$\left(\mathrm{Re}_D = \frac{U_{\max} \cdot D}{\nu}\right) \tag{1}$$

$$\left(U_{\max} = \frac{W}{W - N_{\mathrm{span}} \cdot D} \cdot U_m\right) \tag{2}$$

To begin either flow or heat transfer tests, a coupon was inserted into the testing facility and secured. Before recording data, the test facility was pressurized and then checked for leaks. To obtain a given Reynolds number, a needle valve located downstream of the test section was used to adjust the back pressure.

For the flow test, both inlet and outlet pressures were measured using static pressure taps located upstream of the inlet contraction and downstream of the outlet expansion. During the flow test, the friction factor was calculated using Eq. (3), using the pressure drop each coupon as ΔP. To account for the expansion at the exit of the coupon, a loss coefficient of one was used to calculate the pressure at the coupon exit.

During the heat transfer tests, the same process was used to achieve the target Reynolds number; however, a heated copper block was adhered to the coupon outer walls to impose a constant temperature boundary condition on the coupon. Using a power supply, heat was applied to the heating device that consisted of surface heaters adhered to the copper block with a thin layer of thermally conductive paste. The voltage across the surface heater was measured to calculate the heat into the system. One heating device was attached on each side of the coupon for symmetric heating. For additional adhesion and conduction, a thin layer of thermally conductive paste was administered on the contact area of the copper block and coupon.

To measure temperatures in the facility, thermocouples were inserted in the copper blocks, surface heater, rigid foam, and nylon. Knowing the thermal conductivity of the copper block and the paste, the surface temperature of the coupon was calculated using a one-dimensional (1D) heat transfer analysis; a full description of the 1D conduction analysis can be found in Ref. [33]. Additionally, the thermocouples in the rigid foam and nylon were

used to calculate the conduction losses of the system, which were also calculated using a 1D heat transfer analysis. In the worst case scenarios, at low Reynolds numbers with the widest spaced pins, conduction losses near 17% of the total heat input into the system. However, for all coupons above a Reynolds number of 5000, conduction losses were under 8%.

The heat transfer coefficient was calculated using Eq. (4), where the term ΣQ_{loss} was the sum of all calculated conduction losses. The surface area in the channel was calculated as twice the endwall surface area (top and bottom endwalls) plus twice the side wall surface area, plus the pin surface area, minus twice the pin footprint area (on top and bottom endwalls). The surface area of each pin, and consequently its footprint, was different. However, one suite of tests for this study investigated coupons containing the same wetted surface area. Thermocouples were also located at the inlet and exit to the test coupon. An energy balance was calculated for each test and compared to the measured heat into the system, minus the conduction losses; the two methods compared within 10% for Reynolds numbers above 4000

$$\left(f = \Delta P \frac{1}{2\rho U_{\max}^2} \cdot \frac{1}{N_{\text{rows}}}\right) \tag{3}$$

$$\left(h = \frac{Q_{\text{in}} - \sum Q_{\text{loss}}}{A_s \cdot \Delta T_{\text{lm}}}\right) \tag{4}$$

Uncertainty Analysis. Experimental uncertainty was quantified using the method proposed by Kline and McClintock [42]. Uncertainty was calculated in terms of both overall uncertainty and precision uncertainty using a 95% confidence interval. In the case of the pressure loss tests, the overall uncertainty was dominated by the size of the pressure transducer used to measure the ΔP across the coupon. In the coupons with the widest spanwise spacings, the pressure loss at Reynolds numbers less than 500 was too low to measure accurately and yielded uncertainties nearing 30%. However, pressure loss tests conducted for all coupons with Reynolds numbers over 1000 produced overall uncertainties in friction factor less than 10%; above Reynolds numbers of 5000, the total friction factor uncertainty decreased to less than 6%. Additionally, precision uncertainty for the friction factor results was under 2% for the entire range of Reynolds numbers tested.

For heat transfer tests, the calculation of the coupon surface temperature produced the largest source of uncertainty. Uncertainty in the thermal paste thickness adhering the copper block to the coupon contributed to that uncertainty in surface temperature calculation. Above Reynolds numbers of 3000, the overall uncertainty in Nusselt number remained nearly constant at 5%. However, the Nusselt number results were repeatable to within 3% for all Reynolds numbers.

Results and Discussion

The results of each of the DMLS pin fin arrays from the current study, in addition to four DMLS cylindrical pin fin arrays from Kirsch and Thole [1] for comparison, will be grouped based on spanwise spacing. For a spanwise spacing of $S/D = 1.5$, two different streamwise spacings will be included (listed in Table 2) so that the effects of streamwise spacing can be analyzed directly. An additional grouping will contain the coupons with the same wetted surface area.

Data were analyzed using the same method from Kirsch and Thole [1] and are based on CAD model dimensions, instead of the pin diameters calculated from the CT scans. Based on the CT scanned measurements, changing the pin diameter to the actual dimensions did not affect trends in the results.

With regard to the two different orientations of the triangular pin fins, the nomenclature in the upcoming results will reflect which side of the pin faced the flow. For example, "triangle, point" indicates that the point of the triangle was facing the flow, whereas, "triangle, face" indicates the blunt face of the triangle faced the flow. Table 1 shows these two orientations visually.

Important to note is that the diameter of each geometry dictated the number of pins in the array. Since the stars and dimpled spheres had the largest diameter, they always had fewer pins than the arrays with triangles and cylinders.

Friction factor results will be presented first, followed by the heat transfer performance of the arrays. The combined friction factor and Nusselt number augmentation of the arrays will be presented last; the discussion will include the performance of other pin fin arrays from literature in addition to other common internal cooling schemes.

Pressure Loss Results. For each coupon tested, various Reynolds numbers were set and the resulting friction factor was calculated. Laminar and turbulent friction factor correlations will be included on each graph using laminar theory (16/Re) and Colebrook correlation [43]. To verify the validity of the rig, an aluminum, conventionally machined smooth channel coupon was tested at the beginning and throughout the test campaign to ensure accurate measurements. For the smooth coupon, ε/D_h (channel roughness/hydraulic diameter) was assumed to be zero since the channel walls were reamed smooth. The results from the smooth coupon served as a benchmark and will be included on all of the friction factor graphs.

Figure 4 shows friction factor versus Reynolds number for coupons with $S/D = 4.0$ and $X/D = 2.6$. Triangle pin orientations are included as well as a cylindrical pin fin array from Kirsch and Thole [1]. Performance of the triangle at wide spacing is consistent with literature [16]; Siw et al. [16] found that triangles spaced at $S/D = 3.5$ exhibited a higher friction factor than cylindrical pins at the same spacing. The triangles oriented with the larger blockage facing the inlet (triangle, face) had a larger pressure drop than when the point was oriented toward the inlet (triangle, point). At a Reynolds number around 10,000, the triangle, face array exhibited a friction factor near 50% higher than either the triangle, point and cylindrical pin fin array. The aerodynamic properties of each orientation drove this trend.

Results in Fig. 5 incorporate the same geometries as Fig. 4 along with the dimpled spherical pins and the star pins; all test coupons were spaced at $S/D = 2.0$ and $X/D = 2.6$. The triangles with their faces oriented toward the flow and the cylindrical pins

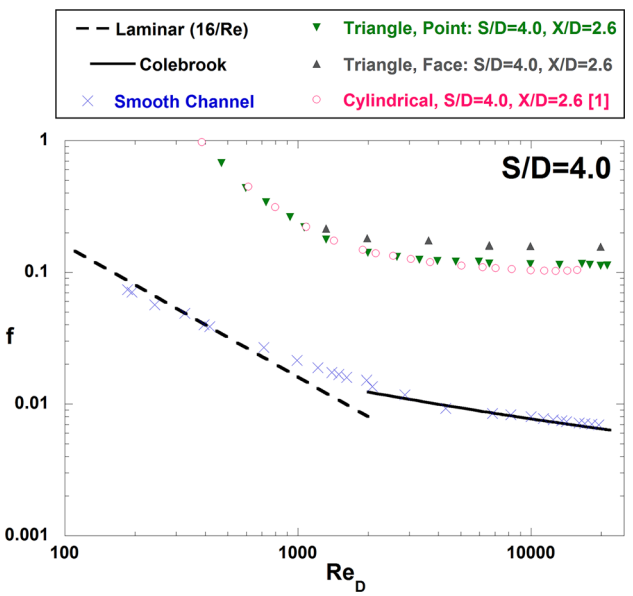

Fig. 4 Friction factor results from coupons with *S/D* = 4.0, *X/D* = 2.6

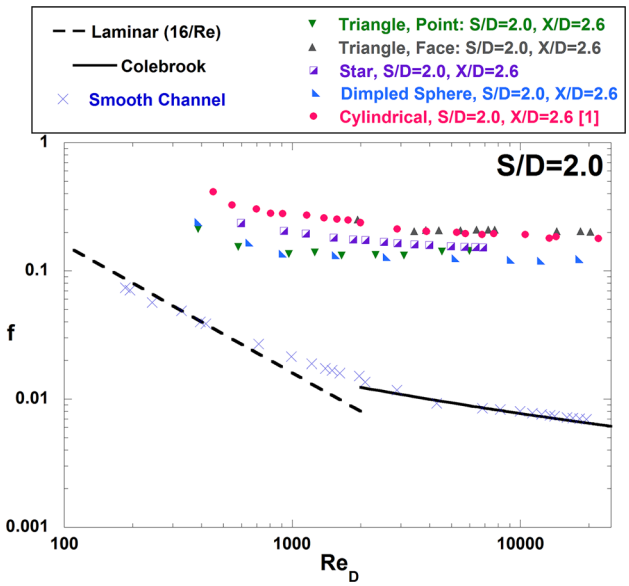

Fig. 5 Friction factor results from coupons with *S/D* = 2.0, *X/D* = 2.6

resulted in the highest friction factor performance. Next came the stars, triangle point, and the dimpled spheres. The cylindrical pin fins had higher friction factors than the triangles oriented with the point facing flow in this dataset, which differed from results in Fig. 4. The dimpled spheres had the lowest friction factors among the data sets, due most likely in part to the shape and lower number of pins in both the spanwise and streamwise dimensions of the array. The stars had the least amount of pins in both streamwise and spanwise dimensions, but a less aerodynamic shape that increased friction factor relative to the dimpled spherical pins.

Figure 6 shows the friction factor performance for the two triangle orientations, star, and cylindrical [1] geometries with $S/D = 1.5$ along with two different streamwise spacings of $X/D = 2.6$ and $X/D = 1.3$. The data display triangles with their face oriented toward flow and cylinders with the highest friction factors. Important to note is that triangles oriented with their point toward the flow outperformed all of the other geometries; their performance is highlighted in the magnified portion of the graph. The star pins performed similarly to the cylindrical pins with wider streamwise spacing.

Since Fig. 6 has two different X/D spacings, the effects of streamwise spacing can be analyzed. Comparing the solid markers with their corresponding open markers shows that friction factor was constant regardless of spacing for the triangles with their points facing the flow. However, for the triangles oriented with their face toward the flow and, to some extent, for the star pins, a slight increase in the friction factor was seen for the tighter streamwise spacing. The difference in effect of streamwise spacing among the different geometries is hypothesized to be related to the size of the wake generated by the pin. Since the triangle, point pins generate smaller wakes than the triangle, face and cylindrical pin fin arrays, interactions between the rough surfaces and pin wakes is limited. As a result, the triangle point is less dependent on streamwise spacing. While streamwise spacing generally does not affect friction factor [8,9], the same streamwise spacing effect was seen for the cylindrical pins and was reported in Ref. [1], citing different levels of roughness in the channels due to the different number of pins in the array. The similarities in results from the triangular and cylindrical pin arrays support the findings from Kirsch and Thole [1] that surface roughness is tied to the number of pin fins in a channel.

Performance of the triangles (point) and cylinders relative to each other was not consistent between Figs. 4 and 6. A comparison of these graphs shows that the triangles oriented with point toward the flow performed better than the cylinders when S/D spacing was less than 4.0. In hypothesizing why this trend exists, we note that as both spanwise and streamwise spacing was decreased, the straight sides of the triangles began to align. As these sides aligned, a flow pattern was created that was similar to channel flow through the triangular elements, which is significantly different than a standard pin fin flowfield with wake effects. This channel-like behavior reduced the friction factor because

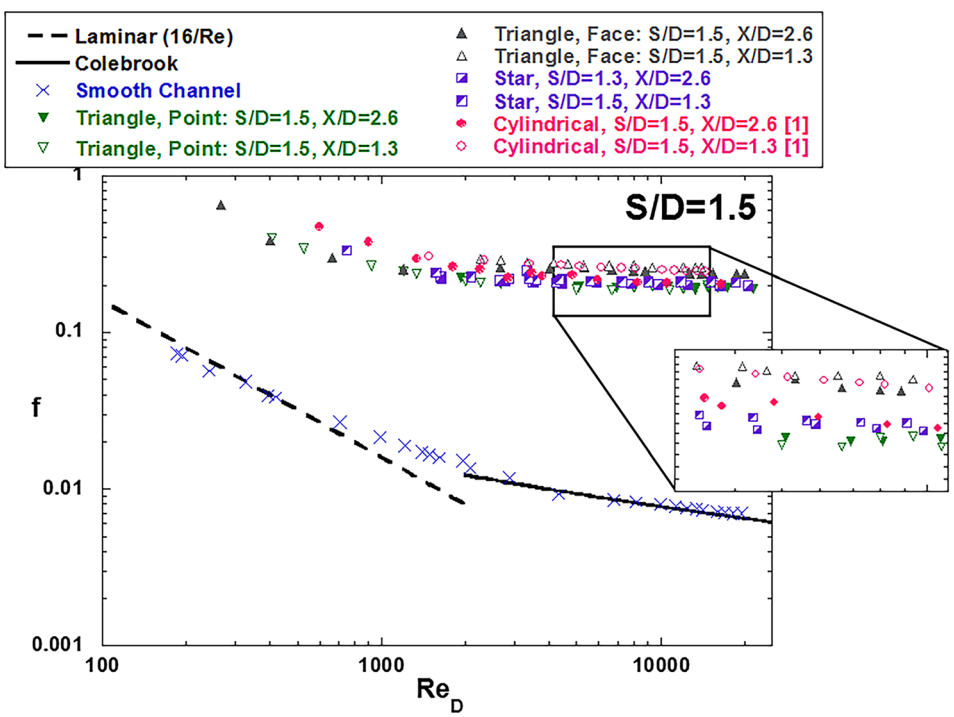

Fig. 6 Friction factor results from coupons with *S/D* = 1.5 and *S/D* = 1.3, and two other streamwise spacings of *X/D* = 1.3 and *X/D* = 2.6

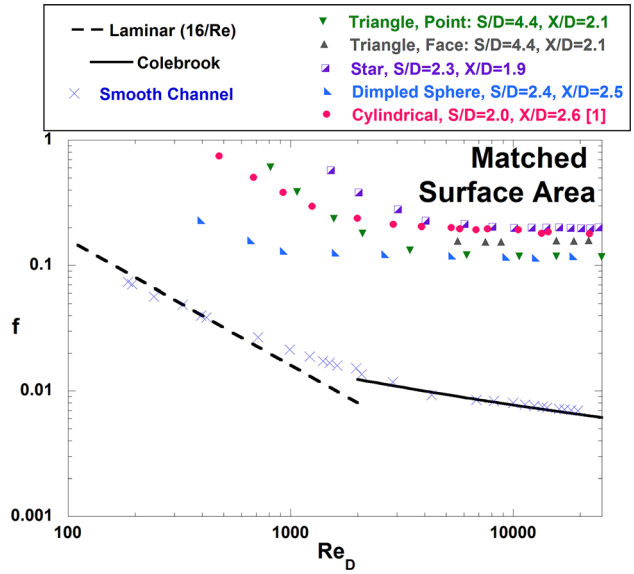

Fig. 7 Friction factor results for coupons containing the same wetted surface area. Both streamwise and spanwise spacing vary among all coupons.

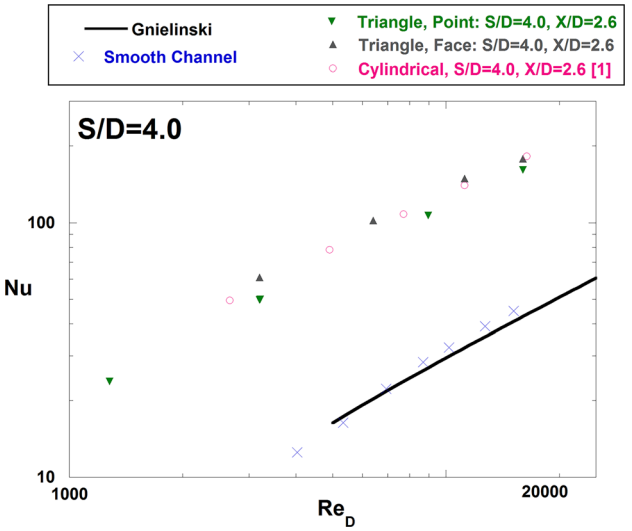

Fig. 8 Heat transfer results for coupons with $S/D = 4.0$, $X/D = 2.0$

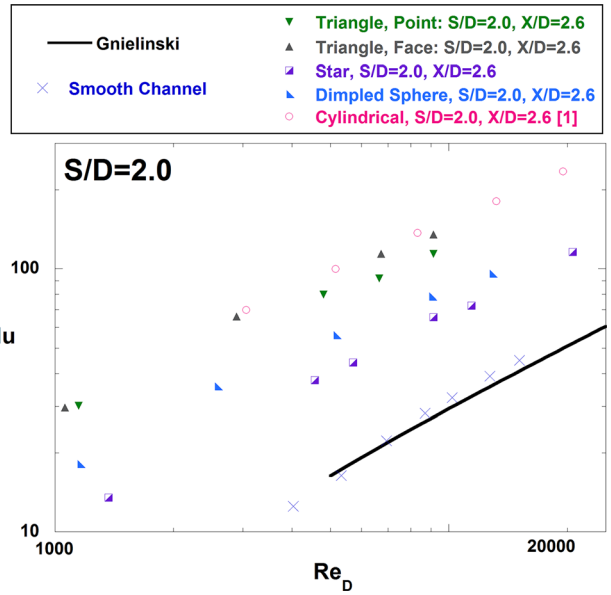

Fig. 9 Heat transfer results for coupons with $S/D = 2.0$, $X/D = 2.6$

wake interaction would have been limited by the pin walls. The cylinders did not experience this phenomena to the same extent because the sides were curved thereby forcing a wake-type flow.

Results in Fig. 7 show the effects with matched surface area for the geometries shown. Spacings for the geometries are listed in Table 2 and were compared with cylinders from Kirsch and Thole [1] spaced at $S/D = 2.0$ and $X/D = 2.6$. An important note is that the number of rows of pins in the spanwise and streamwise dimensions varied in this comparison because the array was based on wetted surface area. The star pins exhibited the highest friction factor, followed by the cylinders, triangles, and dimpled spheres. Triangles oriented with face toward the flow and cylinder geometry had pressure losses that were consistent with one another. This similarity in performance suggests that the flowfields in both geometries were similar. In contrast, when a more aerodynamic configuration was used (triangle, point), friction factor results were lower than for the cylindrical array.

Geometry dominated pressure loss results with a more aerodynamic shape producing lower friction factors; the triangle pin oriented with point facing the flow performed better than the triangles with their face toward flow. Other variables that affected performance included the number of pins in both the spanwise and streamwise dimensions of the array and the streamwise spacing of the pins. Fewer pins in the spanwise dimension represented less of a blockage to the flow, which resulted in lower friction factors. Tighter streamwise spacing, on the other hand, increased friction factor in the triangles oriented with their face toward flow and the stars, which is consistent with the cylinders from Kirsch and Thole [1]. The effects of streamwise spacing can be linked to surface roughness, the levels of which increase with the number of pins in each channel. Trends from the matched surface area coupons were consistent with the relative geometric trends at various spacings, which supports that geometry has the largest influence on friction factor results. Finally, performance of the triangles oriented with face toward the inlet and the cylinders support that the flowfields were similar.

Heat Transfer Results. Heat transfer experiments were set up the same way as pressure drop tests, except a constant temperature boundary condition was imposed on the coupon. Before testing, the rig was validated using the same smooth channel coupon used for the pressure loss tests; results were compared to the Gnielinski correlation [44], which was also used in calculating Nu_0 for the subsequent augmentation analyses. The smooth channel coupon will be included in all results graphs of Nusselt numbers versus Reynolds numbers.

Figure 8 shows heat transfer for both orientations of triangle pin fins and a cylindrical pin fin array from Kirsch and Thole [1] at $S/D = 4.0$ and X/D 2.6 spacings. The cylinders and triangles oriented with the blunt surface facing flow showed similar heat transfer performance and marginally outperformed the triangles with the point facing flow.

Coupons spaced at $S/D = 2.0$ and $X/D = 2.6$ are shown in Fig. 9 and feature the geometries from Fig. 8 along with the star pin fin array and the dimpled spherical pin fin array. The cylinders and triangles with the face oriented toward the flow behaved similarly to data from Fig. 8, and exhibited the highest heat transfer. These geometries were followed by the triangles with the point facing flow, the dimpled spheres, and the stars. The star pins especially showed poor heat transfer, with Nusselt numbers less than one half those seen for the cylindrical pins.

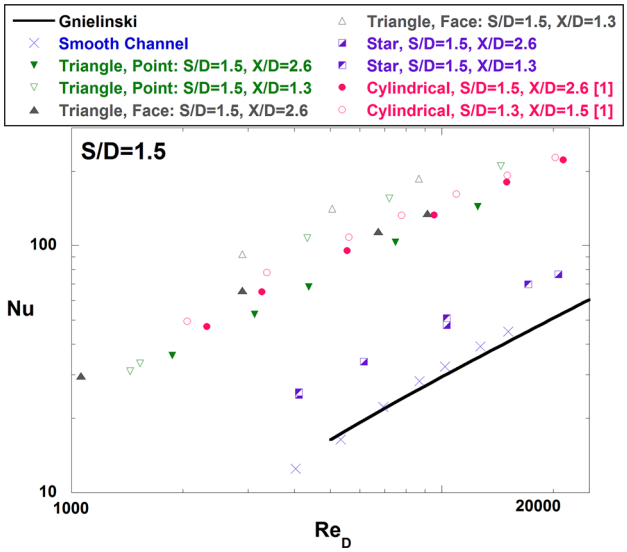

Fig. 10 Heat transfer results for coupons with *S/D* = 1.5, and two streamwise spacings of *X/D* = 2.6 and *X/D* = 1.3

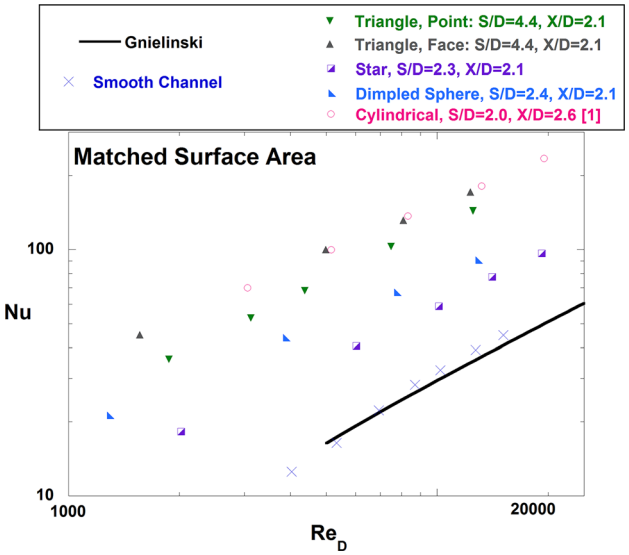

Fig. 11 Heat transfer results for coupons containing the same wetted surface area. Spanwise and streamwise spacing differ among all coupons.

Figure 10 shows the heat transfer performance from all arrays with $S/D = 1.5$; like in Fig. 6, two different streamwise spacings were included as well, $X/D = 2.6$ and $X/D = 1.3$. Triangles oriented with the base facing flow exhibited the highest heat transfer followed in decreasing order by cylinders, triangles oriented with point facing flow, and stars. Comparing different streamwise spacings for each geometry suggests that tighter X/D spacing increased heat transfer performance, which is consistent with results reported in the literature [8,9]. This trend can be explained by the increase of pins in the streamwise dimension of the array that result from decreased spacings. The tighter spacing encouraged stronger wake interactions among the pins. Additionally, relative to the cylinders, the triangles showed a stronger streamwise spacing dependency in Fig. 10; the opposite trend was noted in Fig. 6, where the friction factor of the cylindrical pins showed a stronger streamwise dependence. As previously mentioned, with decreased spanwise and streamwise spacing, the triangle geometry encouraged channel-like flow because the sides of the triangular pins aligned and created more concentrated wake patterns, which would be beneficial to the heat transfer.

Figure 11 features the datasets for matched wetted surface area and can be used to analyze the effect that surface area and geometry have on heat transfer. Both orientations of the triangle array, the star array, and the dimpled spherical array were tested and compared with the cylindrical array from Kirsch and Thole [1]. The triangle array oriented with face toward the inlet and the cylinder array performed similarly, indicating that flowfields in the array were similar. Additionally, the other geometries followed trends seen throughout all the data, with the star array performing the lowest, followed by the dimpled spherical array and then the triangle array oriented with the point toward the inlet. The consistency in performance trends across various spacings suggests that geometry strongly affects the results regardless of whether the surface area or the spacing is matched. The pin shape, and hence its wake shedding characteristics and wake interactions with the endwalls, are integral in determining the heat transfer.

Overall, the stars and dimpled spheres had lower heat transfer performance than the other geometries. The poor performance most likely resulted from the lack of pins in both spanwise and streamwise dimensions in the array; the number of pins in the dimpled spherical pin fin array was about half of that in the cylindrical array. The number of pins had a positive correlation with heat transfer, which explains why the star and dimpled spheres, which always had fewer pins than the other geometries, had lower heat transfer performance. Given that heat transfer is influenced by the wake interactions among the pins, increased spacing in both spanwise and streamwise dimensions limited the wake interactions and therefore lowered the heat transfer.

In Figs. 8–11, heat transfer results from the cylinders and triangles with face oriented toward flow coincided at higher Reynolds numbers. This trend also occurred in Fig. 7 with regard to pressure loss. Since the triangles were able to create a similar flowfield and yield similar heat transfer results with a smaller blockage of flow than the cylinders, the triangles represent a better use of material distribution in a pin fin array.

As with pressure loss, heat transfer performance for the triangles was dependent on shape, with the less aerodynamic triangle exhibiting higher heat transfer. This phenomenon was driven by the increase of obstructed flow that created proportionally larger wakes and larger impingement areas as the flow impacted the face of the triangle. An important heat transfer mechanism in DMLS pin fin arrays is not only the pin wake interactions themselves, which is affected by streamwise spacing [9], but also the wakes' interactions with the rough endwalls. With a higher pin density came an increase in wake interactions, which led to higher heat transfer from the array. In the case of the star pins and the dimpled spheres, the pin density was not enough to promote strong wake interactions and the heat transfer suffered as a consequence.

Augmentation Analysis. A comprehensive understanding of microchannel pin fin array performance can be achieved by comparing friction factor augmentation to heat transfer augmentation. To optimize performance, heat transfer benefits should outweigh penalties in pressure losses. Figure 12 shows the results from the current study, along with a study containing straight DMLS microchannels from Stimpson et al. [33] and some previous studies from the literature containing pin fins [8,45] and ribs [46]. Large, solid markers identify the DMLS shaped pin fins, while smaller, open markers identify the studies from previous work. For clarity, the data sets were grouped by geometry and not separated by spacing; the spacing of the triangle pins oriented with their face toward the flow is highlighted where the geometry far outperforms the others.

Results indicate that the triangles and cylinders performed the best relative to the stars and dimpled spheres. The largest heat transfer augmentation occurred when the triangles oriented with their face toward the flow were spaced at $S/D = 1.5$, which reinforces the observation that triangles perform better at tighter

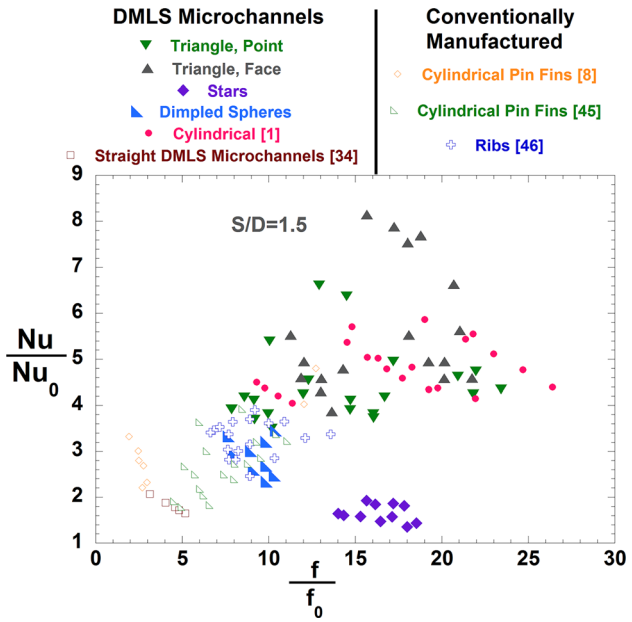

Fig. 12 Friction factor augmentation versus Nusselt number augmentation for all DMLS microchannels from the current study, straight DMLS microchannels [33], and conventionally manufactured (relatively smooth walled) studies containing pin fins [8,45], and ribs [46]

spacings. In addition to the previous orientation, the cylinders and triangles oriented with the point facing flow had notable performances. The dimpled spheres performed similarly to conventionally manufactured pin fin arrays and ribbed channels from previous studies. Finally, the stars had low heat transfer benefits and showed poor heat transfer performance for a substantial pressure loss.

Conclusions

Three unique pin geometries were printed using DMLS and compared to DMLS cylindrical pin fin arrays from Kirsch and Thole [1]. Tests were conducted to study the effects that geometry, spacing, and number of pin fins had on pressure loss and heat transfer.

Results from this study suggest that geometry has the most prominent effect on both pressure loss and heat transfer relative to spacing of the pin fins. The triangular and cylindrical geometries exhibited the highest heat transfer augmentation, with the triangles oriented with the face toward flow creating the highest. The star and dimpled sphere geometry had poor overall performance. The effects of streamwise spacing were small but measureable for friction factor, especially for the triangular pins oriented with their face toward the flow. However, streamwise spacing directly affected heat transfer and was positively correlated with the heat transfer performance, with decreased spacing resulting in increased heat transfer.

As the spacings between pin fins decreased, more pins fit in the coupon. This suggests that the increase in friction factor caused by spanwise spacing and increase in heat transfer caused by streamwise spacing was related to the number of pins in both the spanwise and streamwise distances. Since each geometry had a different diameter, the number of pins varied in each array. The stars and dimpled spheres had the least amount of pins in the matched surface area data set and also exhibited the lowest heat transfer. Unless the spacing of those pins can be tightened, thereby introducing more pins in both spanwise and streamwise dimensions, these geometries would be a poor choice to use for a pin fin array.

To optimize internal cooling schemes, the benefits of heat transfer need to outweigh losses from friction. The test suite containing arrays with the same wetted surface area showed that the cylindrical pins and triangular pins performed similarly. Given that the triangular pins were smaller than the cylindrical pins, implementing triangular pin fins instead of cylindrical pins could lead to weight savings in a part. For applications where a large pressure drop is acceptable, DMLS microchannel pin fin arrays containing triangular shaped pins provide excellent heat transfer performance.

More research needs to be conducted to fully understand additively manufactured pin fins and to optimize the types of finned heat exchangers. To better understand how geometry affects pressure loss and heat transfer, the additive manufacturing process can be leveraged to build unique shapes that can be tested at a variety of spacings. With further research on additively manufactured pin fin arrays, insights into the interrelated effects of surface roughness, pin shape, and pin spacing can lead to more effective heat exchangers.

Acknowledgment

All test coupons were manufactured at Penn State's CIMP-3D Laboratory by Corey Dickman and Griffin Jones. The CT scans were performed by Jacob Snyder, from the START Laboratory. The authors are incredibly grateful for the help of these individuals; without their efforts, these studies would not have been possible.

Nomenclature

A_c = cross-sectional flow area
A_s = wetted surface area
D = pin diameter
D_h = hydraulic diameter; $(4A_c/p)$
f = Fanning friction factor
f_0 = smooth channel friction factor, Colebrook equation; $(f_0^{1/2} = -2.0 \cdot \log((\varepsilon/D)/3.7 + 2.51 \cdot (\mathrm{Re}_{Dh} \cdot f^{1/2}))^{-1})$
h = convective heat transfer coefficient
H = channel height
k = thermal conductivity
L = coupon length
N_{rows} = number of rows
N_{span} = number of pins in the spanwise dimension
Nu = Nusselt number; (hD_h/k_{air})
p = perimeter
P = static pressure
Q = heat transfer rate
R_a = arithmetic mean surface roughness; $((1/n)\sum_{i=1}^{n} |z_{\mathrm{surf}} - z_{\mathrm{meas}}|)$
Re_D = pin Reynolds number; $(U_{\max} D_h/\upsilon)$
$\mathrm{Re}_{\mathrm{Dh}}$ = channel Reynolds number; (UD_h/υ)
S = spanwise distance
T = static temperature
U = fluid velocity
W = channel width
X = streamwise distance

Greek Symbols

Δ = differential
ν = kinematic viscosity
ρ = density

Subscripts

lm = log mean
m = mean
s = surface
0 = reference condition
1 = inlet
2 = exit

References

[1] Kirsch, K. L., and Thole, K. A., 2017, "Pressure Loss and Heat Transfer for Additively and Conventionally Manufactured Pin Fin Arrays," Int. J. Heat Mass Transfer, **108**(Pt. B), pp. 2502–2513.
[2] Chyu, M. K., and Moon, H. K., 2009, "Effects of Height-to-Diameter Ratio of Pin Element on Heat Transfer From Staggered Pin-Fin Arrays," ASME Paper No. GT2009-59814.

[3] VanFossen, G. J., 1982, "Heat-Transfer Coefficients for Staggered Arrays of Short Pin Fins," ASME J. Eng. Power, **104**(2), pp. 268–274.
[4] Brigham, B. A., and VanFossen, G. J., 1984, "Length to Diameter Ratio and Row Number Effects in Short Pin Fin Heat Transfer," ASME J. Eng. Gas Turbines Power, **106**(1), pp. 241–244.
[5] Simoneau, R. J., and VanFossen, G. J., 1984, "Effect of Location in an Array on Heat Transfer to a Short Cylinder in Crossflow," ASME J. Heat Transfer, **106**(1), pp. 42–48.
[6] Metzger, D. E., Fan, C. S., and Haley, S. W., 1984, "Effects of Pin Shape and Array Orientation on Heat Transfer and Pressure Loss in Pin Fin Arrays," ASME J. Eng. Gas Turbines Power, **106**(1), pp. 252–257.
[7] Lyall, M. E., Thrift, A. A., Thole, K. A., and Kohli, A., 2011, "Heat Transfer From Low Aspect Ratio Pin Fins," ASME J. Turbomach, **133**(1), p. 011001.
[8] Lawson, S. A., Thrift, A. A., Thole, K. A., and Kohli, A., 2011, "Heat Transfer From Multiple Row Arrays of Low Aspect Ratio Pin Fins," Int. J. Heat Mass Transfer, **54**(2011), pp. 4099–4109.
[9] Ostanek, J. K., and Thole, K. A., 2012, "Flowfield Interactions in Low Aspect Ratio Pin-Fin Arrays," ASME J. Turbomach, **134**(5), p. 051034.
[10] Ostanek, J. K., and Thole, K. A., 2012, "Effects of Varying Streamwise and Spanwise Spacing in Pin Fin Arrays," ASME Paper No. GT2012-68127.
[11] Han, J. C., Dutta, S., and Ekkad, S. V., 2000, *Gas Turbine Heat Transfer and Cooling Technology*, Taylor & Francis, New York.
[12] Uzol, O., and Camci, C., 2005, "Heat Transfer, Pressure Loss and Flow Field Measurements Downstream of Staggered Two-Row Circular and Elliptical Pin Fin Arrays," ASME J. Heat Transfer, **127**(5), pp. 458–471.
[13] Chyu, M. K., Hsing, Y. C., and Natarajan, V., 1998, "Convective Heat Transfer of Cubic Fin Arrays in a Narrow Channel," ASME J. Turbomach., **12**(2), pp. 362–367.
[14] Kirsch, K. L., Ostanek, J. K., Thole, K. A., and Kaufman, E., 2014, "Row Removal Heat Transfer Study for Pin Fin Arrays," ASME Paper No. GT2014-25348.
[15] İzci, T., Koz, M., and Kosar, A., 2015, "The Effect of Micro Pin-Fin Shape on Thermal and Hydraulic Performance of Micro Pin-Fin Heat Sinks," Heat Transfer Eng., **36**(17), pp. 1447–1457.
[16] Siw, S. C., Chyu, M. K., and Alvin, M. A., 2012, "Heat Transfer Enhancement of Internal Cooling Passage With Triangular and Semi-Circular Shaped Pin-Fin Arrays," ASME Paper No. GT2012-69266.
[17] Marques, C., and Kelly, K. W., 2004, "Fabrication and Performance of a Pin Fin Micro Heat Exchanger," ASME J. Heat Transfer, **126**(3), pp. 434–444.
[18] Heo, K. Y., Kihm, K. D., and Lee, J. S., 2014, "Fabrication and Experiment of Micro-Pin-Finned Microchannels to Study Surface Roughness Effects on Convective Heat Transfer," J. Micromech. Microeng., **24**(12), p. 125025.
[19] Cormier, Y., Dupuis, P., Farjam, A., Corbeil, A., and Jodoin, B., 2014, "Additive Manufacturing of Pyramidal Pin Fins: Height and Fin Density Effects Under Forced Convection," Int. J. Heat Mass Transfer, **75**, pp. 235–244.
[20] Dupuis, P., Cormier, Y., Fenech, M., Corbeil, A., and Jodoin, B., 2016, "Flow Structure Identification and Analysis in Fin Arrays Produced by Cold Spray Additive Manufacturing," Int. J. Heat Mass Transfer, **93**, pp. 301–313.
[21] Dupuis, P., Cormier, Y., Fenech, M., and Jodoin, B., 2016, "Heat Transfer and Flow Structure Characterization for Pin Fins Produced by Cold Spray Additive Manufacturing," Int. J. Heat Mass Transfer, **98**, pp. 650–661.
[22] Dede, E. M., Joshi, S. N., and Zhou, F., 2015, "Topology Optimization, Additive Layer Manufacturing, and Experimental Testing of an Air-Cooled Heat Sink," ASME J. Mech. Des., **137**(11), p. 111403.
[23] Jamshidinia, M., and Kovacevic, R., 2015, "The Influence of Heat Accumulation on the Surface Roughness in Powder-Bed Additive Manufacturing," Surf. Topogr. Metrol. Prop., **3**(1), p. 014003.
[24] Bacchewar, P. B., Singhal, S. K., and Pandey, P. M., 2007, "Statistical Modelling and Optimization of Surface Roughness in the Selective Laser Sintering Process," Proc. Inst. Mech. Eng. Part B, **221**(1), pp. 35–52.
[25] Wegner, A., and Witt, G., 2012, "Correlation of Process Parameters and Part Properties in Laser Sintering Using Response Surface Modeling," Phys. Procedia, **39**, pp. 480–490.
[26] Yadroitsev, I., and Smurov, I., 2011, "Surface Morphology in Selective Laser Melting of Metal Powders," Phys. Procedia, **12**(**1**), pp. 264–270.
[27] Khaing, M. W., Fuh, J. Y. H., and Lu, L., 2001, "Direct Metal Laser Sintering for Rapid Tooling: Processing and Characterisation of EOS Parts," J. Mater. Process. Technol., **113**(1–3), pp. 269–272.
[28] Delgado, J., Ciurana, J., and Rodríguez, C. A., 2012, "Influence of Process Parameters on Part Quality and Mechanical Properties for DMLS and SLM With Iron-Based Materials," Int. J. Adv. Manuf. Technol., **60**(5–8), pp. 601–610.
[29] Strano, G., Hao, L., Everson, R. M., and Evans, K. E., 2013, "Surface Roughness Analysis, Modelling and Prediction in Selective Laser Melting," J. Mater. Process. Technol., **213**(4), pp. 589–597.
[30] Snyder, J. C., Stimpson, C. K., Thole, K. A., and Mongillo, D., 2016, "Build Direction Effects on Additively Manufactured Channels," ASME J. Turbomach., **138**(5), p. 051006.
[31] Pakkanen, J., Calignano, F., Trevisan, F., Lorusso, M., Ambrosio, E. P., Manfredi, D., and Fino, P., 2016, "Study of Internal Channel Surface Roughnesses Manufactured by Selective Laser Melting in Aluminum and Titanium Alloys," Metall. Mater. Trans. A, **47**(8), pp. 3837–3844.
[32] Ning, Y., Wong, Y. S., Fuh, J. Y. H., and Loh, H. T., 2006, "An Approach to Minimize Build Errors in Direct Metal Laser Sintering," IEEE Trans. Autom. Sci. Eng., **3**(1), pp. 73–80.
[33] Stimpson, C. K., Snyder, J. C., Thole, K. A., and Mongillo, D., 2016, "Roughness Effects on Flow and Heat Transfer for Additively Manufactured Channels," ASME J. Turbomach., **138**(5), p. 051008.
[34] Kirsch, K. L., and Thole, K. A., 2016, "Heat Transfer and Pressure Loss Measurements in Additively Manufactured Wavy Microchannels," ASME J. Turbomach, **139**(1), p. 011007.
[35] Stimpson, C. K., Snyder, J. C., and Thole, K. A., 2016, "Scaling Roughness Effects on Pressure Loss and Heat Transfer of Additively Manufactured Channels," ASME J. Turbomach., **139**(2), p. 021003.
[36] Grimm, T., Wiora, G., and Witt, G., 2015, "Characterization of Typical Surface Effects in Additive Manufacturing With Confocal Microscopy," Surf. Topogr. Metrol. Prop., **3**(1), p. 014001.
[37] Xue, L., Li, Y., Chen, J., and Wang, S., 2015, "Laser Consolidation—A Novel Additive Manufacturing Process for Making Net-Shape Functional Metallic Components for Gas Turbine," ASME Paper No. GT2015-43971.
[38] EOS GmbH, 2014, "Material Data Sheet—EOS NickelAlloy IN718," EOS GmbH-Electro Optical Systems, Krailling, Germany, accessed Oct. 17, 2017, http://ip-saas-eos-cms.s3.amazonaws.com/public/4528b4a1bf688496/ff974161c2057e6df56db5b67f0f5595/EOS_NickelAlloy_IN718_en.pdf
[39] Incropera, F. P., DeWitt, D. P., Bergman, T. L., and Lavine, A. S., 2007, *Fundamentals of Heat and Mass Transfer*, Wiley, New York.
[40] Weaver, S. A., Barringer, M. D., and Thole, K. A., 2011, "Microchannels With Manufacturing Roughness Levels," ASME J. Turbomach., **133**(4), p. 041014.
[41] AliCat, 2014, "Mass Flow Controller—Operating Manual," AliCat Scientific, Inc., Tucson, AZ.
[42] Kline, S. J., and McClintock, F. A., 1953, "Describing the Uncertainties in Single Sample Experiments," Mech. Eng., **75**, pp. 3–8.
[43] Colebrook, C. F., and White, C. M., 1937, "Experiments With Fluid Friction in Roughened Pipes," Proc. R. Soc. London A, **161**(906), pp. 367–381.
[44] Gnielinski, V., 1975, "New Equations for Heat and Mass Transfer in Turbulent Pipe and Channel Flow," Int. Chem. Eng., **16**(2), pp. 359–368.
[45] Ostanek, J. K., 2012, "Flowfield Interactions in Low Aspect Ratio Pin-Fin Arrays," Ph.D. dissertation, Pennsylvania State University, State College, PA.
[46] Wright, L. M., Fu, W. L., and Han, J. C., 2004, "Thermal Performance of Angled, V-Shaped, and W-Shaped Rib Turbulators in Rotating Recatangular Cooling Channels (AR=4:1)," ASME J. Turbomach., **126**(4), pp. 604–614.